
A JOINT BAYESIAN SPACE-TIME MODEL TO INTEGRATE SPATIALLY MISALIGNED AIR POLLUTION DATA IN R-INLA

A PREPRINT

C. Forlani*

MRC Centre for Environment and Health
Department of Epidemiology and Biostatistics
School of Public Health
Imperial College London
London, UK

S. Bhatt

Department of Infectious Disease Epidemiology
School of Public Health
Imperial College London
London, UK

M. Cameletti

Department of Management
Economics and Quantitative Methods
Università degli Studi di Bergamo
Bergamo, Italy

E. Krainski

Department of Statistics
Universidade Federal do Paraná
Paraná, Brazil

M. Blangiardo

MRC Centre for Environment and Health
Department of Epidemiology and Biostatistics
School of Public Health
Imperial College London
London, UK

December 24, 2021

ABSTRACT

In air pollution studies, dispersion models provide estimates of concentration at grid level covering the entire spatial domain, and are then calibrated against measurements from monitoring stations. However, these different data sources are misaligned in space and time. If misalignment is not considered, it can bias the predictions. We aim at demonstrating how the combination of multiple data sources, such as dispersion model outputs, ground observations and covariates, leads to more accurate predictions of air pollution at grid level. We consider nitrogen dioxide (NO₂) concentration in Greater London and surroundings for the years 2007-2011, and combine two different dispersion models. Different sets of spatial and temporal effects are included in order to obtain the best predictive capability. Our proposed model is framed in between calibration and Bayesian melding techniques for data fusion red. Unlike other examples, we jointly model the response (concentration level at monitoring stations) and the dispersion model outputs on different scales, accounting for the different sources of uncertainty. Our spatio-temporal model allows us to reconstruct the latent fields of each model component, and to predict daily pollution concentrations. We compare the predictive capability of our proposed model with other established methods to account for misalignment (e.g. bilinear interpolation), showing that in our case study the joint model is a better alternative.

Keywords data integration · coregionalization model · geostatistical model · NO₂ · SPDE

*Correspondence to: c.forlani@imperial.ac.uk

1 Introduction

Air pollution is a major concern for policy makers worldwide (European Commission, 2018; EPA, 2016; WHO, 2006), and there is extensive evidence of its negative effects, in particular on respiratory and cardiovascular diseases (Dominici *et al.*, 2010; COMEAP, 2015; Atkinson *et al.*, 2015; Lipfert, 2017). Obtaining an accurate estimate of air pollution concentration is key for evaluating compliance with regulatory standards set by national and international environmental agencies and to reduce exposure misclassification in epidemiological studies (Berrocal *et al.*, 2012; Shaddick *et al.*, 2017; Keller and Peng, 2019).

Air pollution data come from different sources, each presenting some limitations: ground measurements from monitoring network stations, usually affected by sparse spatial resolution; estimates from Land Use Regression models (LUR), which rely on the availability of accurate and dense monitor observations; satellite remote sensing data, sometimes poorly correlated with ground pollution level; simulations from deterministic models (e.g. chemical transport models or dispersion models), that can present prediction quality concerns despite the complete spatial coverage and high temporal resolution (Shaddick and Wakefield, 2002; Lee *et al.*, 2011; Gelfand *et al.*, 2012; Shaddick *et al.*, 2015; Hoek *et al.*, 2008; Johnson *et al.*, 2010; Chang, 2016; Shaddick *et al.*, 2017).

Several ‘hybrid’ approaches have been proposed to combine these data sources to draw from their strengths and to overcome their limitations, but not all of them address the discrepancy in the spatial resolution of the different data sources, which is known as *misalignment* or *change of support problem* (COSP).

1.1 Main approaches to address spatial misalignment

In the context of COSP, we refer to upscaling methods when the target resolution is lower than the data resolution (e.g. point-to-area), and to downscaling when the target resolution is higher (e.g. area- or grid-to-point).

Model-based solutions for *data assimilation* (also referred to as *data fusion* or *data blending*) in environmental applications allow us to account for all sources of uncertainty while addressing COSP. These are usually set within a hierarchical Bayesian framework. Popular approaches include Bayesian melding and calibration techniques (Chang, 2016).

Bayesian melding assumes that both measurements and modelled data are error-prone realizations of an underlying latent true pollution field, and they both inform the posterior distribution of the latent process. Among the proposed melding strategies applied to misaligned air pollution data we find, for instance, the downscaling spatial Bayesian melding model by Raftery and Fuentes (2005), the upscaling spatial Bayesian melding model by Wikle and Berliner (2005), and the upscaling spatio-temporal fusion model by McMillan *et al.* (2010).

Calibration techniques assume that the model-based estimates (e.g. from dispersion models) are used in a regression framework as predictors against the monitoring site measurements. In this way the computational cost is reduced compared to melding, as the models only need to be fitted at the monitoring sites locations (Berrocal *et al.*, 2012; Chang, 2016). Some examples are the block-averaging upscaling calibration fusion model by Sahu *et al.* (2010), and the spatio-temporal downscaling calibration models by Berrocal *et al.* (2010, 2012), which can be considered a generalization of a Bayesian universal kriging model (Berrocal, 2019).

1.2 Novelty of our approach

In this paper, we are framed in the context of data integration to improve air pollution predictions at a fine grid. We combine monitoring measurements and numerical model outputs coming from two dispersion models, the Pollution Climate Mapping (PCM) from DEFRA (DEFRA, 2018; Ricardo Energy & Environment, 2017) model and the Air Quality Unified Model (AQUM) from the Met Office (Savage *et al.*, 2013; Met Office, 2018), and account for their associated errors.

These deterministic models have previously been used for similar purposes: Lee and Sarran (2015) provide an example of point-to-area upscaling from the PCM model grid to local authority areas for epidemiological applications and Mukhopadhyay and Sahu (2017) combine the AQUM and the monitoring observations to accurately predict NO₂ concentration in UK.

However, usually in the literature only one extra data source at a time is considered (Wikle and Berliner, 2005; Raftery and Fuentes, 2005; McMillan *et al.*, 2010; Sahu *et al.*, 2010; Berrocal *et al.*, 2010, 2012; Zidek *et al.*, 2012; Huang *et al.*, 2015; Lee and Sarran, 2015; Pannullo *et al.*, 2016; Mukhopadhyay and Sahu, 2017; Lee *et al.*, 2017; Huang *et al.*, 2017; Moraga *et al.*, 2017). We show that, when more are available, these can all be put together to get better predictions while accounting for the bias which affects deterministic data.

Our approach is similar to the coregionalization model proposed by Schmidt and Gelfand (2003) to model CO, NO, and NO₂ which allows us to calibrate the deterministic models against the monitor observations through a coefficient similarly to calibration techniques. However, here we treat the three sources of information on NO₂ as coming from the same true underlying spatio-temporal process (i.e. the true air pollution concentration field) as in Bayesian melding. The pure application of this kind of models is computationally prohibitive for the high resolution output data we have at hand. This issue is solved by representing the spatially continuous fields as solutions to a Stochastic Partial Differential Equation (SPDE) to handle this in a computationally efficient way (Lindgren *et al.*, 2011; Krainski *et al.*, 2018).

Additionally, our model reconstructs the continuous latent spatial and temporal fields allowing us to account for all the sources of uncertainty: first, the one associated with the estimates from the numerical models, which is not provided as they are deterministic models, and second, the measurement error associated with ground observations. This is most useful in the perspective of using the predictions from the air pollution model as a measure of exposure in an epidemiological model, where the uncertainty could be fed forward (see for example Lee *et al.* 2017 and Cameletti *et al.* 2019).

The inference is done under the Bayesian paradigm through the Integrated Nested Laplace Approximations (INLA) coupled with the SPDE approach, which is implemented in the R-INLA package (Rue, 2018).

Other authors have implemented solutions for spatially misaligned air pollution data in R-INLA, however their approaches differ from ours under several points of view. In particular, Moraga *et al.* (2017) show an example of area-to-point misalignment addressed via block averaging, in a spatial-only context, without accounting for the uncertainty associated with the raster data. Cameletti *et al.* (2019) implement a spatial upscaler from point to area comparing two different averaging methods. Kifle *et al.* (2017) compare additive and coupled spatio-temporal processes for multivariate data in a biological context (prevalence of vectors for arboviruses), where the data are not misaligned, and do not include any explanatory covariate.

To the best of our knowledge, this is the first time a spatio-temporal model for spatially misaligned point-referenced data is implemented through the INLA-SPDE approach considering more than one deterministic model output at different spatial and temporal resolutions.

We compare and contrast several models and through a cross-validation method we evaluate which one produces the most accurate predictions of NO₂ concentration in Greater London and surroundings for the period 2007 to 2011. We compare our method with two approaches in which the alignment is done through bilinear interpolation or kriging, hence not accounting for the measurement error associated with the misaligned covariates. The first is a simple hierarchical model that includes linear effects for the covariates and structured spatio-temporal residuals. The second is the recently proposed data integration model from Mukhopadhyay and Sahu (2017), which allows for non-stationarity in the residual spatial process.

The remainder of the article is organised as follows: section 2 presents the study area and data; section 3 describes the methods used in the analysis, starting with the model specification followed by a description of the competitor models; section 4 reports the results of the application of such methods to our air pollution data; finally, section 5 contains the conclusions and a short discussion, pointing towards further developments.

2 Study area and data

The study focuses on NO₂, as it is one of the pollutants regulated by national and international directives, and it is traffic driven, hence characterised by high spatio-temporal variability.

We used daily averages of hourly observations from different monitoring networks including the AEA and the Automatic Urban and Rural Network (AURN) from the DEFRA’s UK Air Quality Archive, and the London Air Quality Network (LAQN) in Greater London and surroundings, managed by the King’s College London Environmental Research Group (ERG). The combined database was built as part of the Spatio/Temporal Exposure Assessment Methods (STEAM) project (King’s College London ERG, 2016).

We also considered the outputs of two deterministic models: (i) annual 1km×1km predictions from the PCM model provided by DEFRA (DEFRA, 2018), for 2007-2011; (ii) daily 12km×12km predictions from the AQUM model, available for the years 2007-2011, provided by the Met Office (Met Office, 2018).

We consider the period 2007-2011 due to the availability of the AQUM data.

Among the 213 monitoring stations active between 01/01/2007 and 31/12/2011 for at least 1370 consecutive days (75% of the total number of days), 126 have been included in the analysis after applying the following criteria to the NO₂ time series: (i) the daily average is computed only for the days where at least 18 hourly observations, i.e. the 75%, are

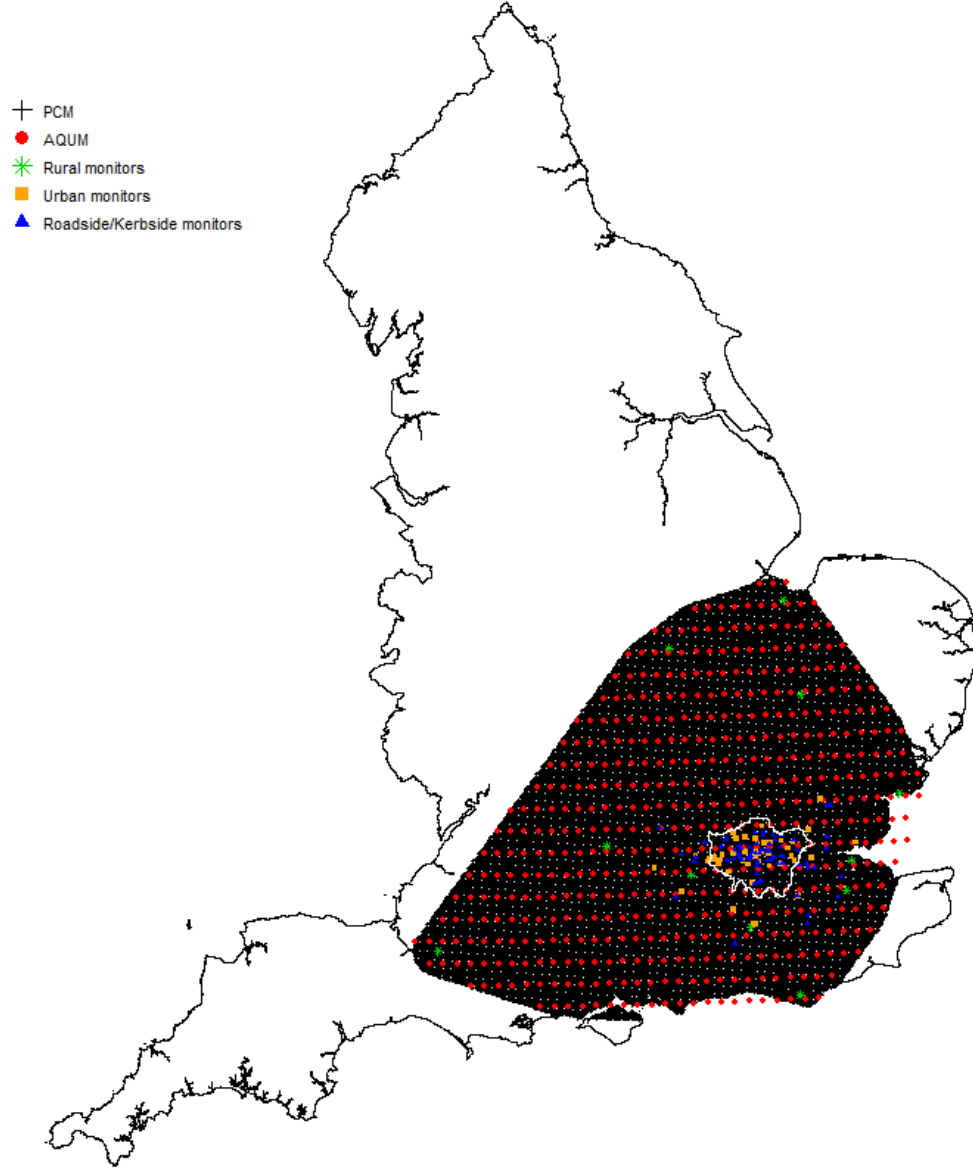


Figure 1: NO₂ data locations on the study domain, on the shape of England as reference.

present; (ii) we eliminated non-positive daily averages which do not allow for the logarithmic transformation required in the analysis (negative observations are due to measurement error); (iii) monitors where the resulting daily NO₂ is available for less than 1370 days, not necessarily consecutive, have been excluded (this is because an active monitor does not necessarily record NO₂ measurements).

The monitors are split into 6 groups maximizing similarity criteria between groups, and a 6-fold cross validation is performed.

For each monitor we have information about the site type classification, that we aggregated into 3 categories: rural, urban, road-kerb side.

We define our study area as that including all the selected monitors, containing 495 grid cells for AQUM and 44,117 grid cells for PCM.

The locations of the air pollution data sources described above are displayed in Figure 1.

Table 1: Descriptive statistics of NO₂ concentration ($\mu\text{g}/\text{m}^3$) for the three data sources

Data	Min	1st Qu.	Median	Mean	3rd Qu.	Max
PCM 2007	7.276	9.948	11.289	13.039	14.055	66.036
PCM 2008	5.615	9.107	10.439	12.064	13.198	56.123
PCM 2009	7.097	10.105	11.333	12.844	13.915	53.290
PCM 2010	5.613	10.396	11.843	13.404	14.705	62.190
PCM 2011	5.437	9.905	11.317	12.545	13.575	55.400
AQUM January	0.215	11.354	19.926	21.943	30.150	73.654
AQUM February	0.154	13.912	22.491	25.052	33.535	97.435
AQUM March	0.291	10.165	16.760	19.180	25.969	84.589
AQUM April	0.059	9.982	15.339	17.248	22.457	81.498
AQUM May	0.008	6.847	10.340	12.187	15.622	77.623
AQUM June	0.000	6.493	9.568	11.088	13.974	63.689
AQUM July	0.409	5.855	8.388	9.842	12.244	67.893
AQUM August	0.000	6.392	9.210	10.591	13.176	58.456
AQUM September	0.054	7.545	11.795	13.899	18.095	68.396
AQUM October	0.067	10.521	16.622	18.402	24.576	70.455
AQUM November	0.531	11.714	18.694	20.942	28.109	97.137
AQUM December	0.000	12.890	23.150	25.040	34.480	121.320
Monitors RUR	0.484	5.357	8.995	11.405	14.734	114.375
Monitors URB	0.679	11.938	19.091	22.286	29.049	166.792
Monitors RKS	0.245	20.208	30.524	34.903	44.422	231.292

The AQUM model includes chemistry, physical and aerosol models, meteorological configuration based on the Met Office’s North Atlantic and European Model (NAE) and emission data (Savage *et al.*, 2013); the PCM model input includes emission inventory, energy projections, road traffic counts, road transport activity and meteorological hourly data from Waddington weather station (Ricardo Energy & Environment, 2017).

Although data were available, we decided against the inclusion of meteorological variables in our models, as they are already an input for both the numerical models considered in the analysis.

Consistently with the selection criteria, all the 6 training and validation sets have similar distribution of daily NO₂ concentration by site type (see Appendix A, Fig. A.1). As expected, in all sets the road-kerb side monitors have higher mean and maximum levels of NO₂.

In particular, 17 road-kerb side sites overcome the limits set by the WHO and the European Commission for the annual average of $40\mu\text{g}/\text{m}^3$, for at least 4 of the 5 years under study (see Appendix A, Fig. A.2). Of these, the monitor in Lambeth-Brixton Road (LB4) is also well above the threshold of $18\mu\text{g}/\text{m}^3$ not to be exceeded more than 18 times annually, for every year, even though a decreasing trend can be observed (from 865 hourly exceedances in 2007, to 62 in 2011), and other 6 monitors exceeded this threshold between 2007 and 2008.

Table 1 reports summary statistics for PCM data by year, AQUM data by month and monitor observations by site type.

3 Methods

In this section we first present some analysis on the AQUM and PCM data, then we introduce the joint model, and finally the models that we use for comparison. Note that we will represent vector/matrices in bold typeface.

3.1 Separate models for AQUM and PCM data

In order to quantify the relevance of the temporal component for PCM ($i = 1$) and the spatial component for AQUM ($i = 2$), we ran three models for each data source separately: (i) one with spatial-only or temporal-only effect respectively, (ii) one with additive spatial and temporal effects and (iii) one with a spatio-temporal interaction.

Let’s define \mathbf{y}_i as the vector of air pollution concentration on the logarithmic scale across space and time for the i -th numerical model. This is assumed to be normally distributed with mean $\boldsymbol{\eta}_i$ and variance $\sigma_{\epsilon_i}^2$: $\mathbf{y}_i \sim MVN(\boldsymbol{\eta}_i, \sigma_{\epsilon_i}^2 I)$

Each element of the linear predictor η_i (for a time point t and location \mathbf{s} identified by UTM coordinates) for models (i), (ii), (iii) is specified as follows:

$$\begin{aligned}\eta_1(\mathbf{s}) &= \alpha_1 + z_{11}(\mathbf{s}) \\ \eta_2(t) &= \alpha_2 + z_{22}(t)\end{aligned}\tag{i}$$

$$\begin{aligned}\eta_1(\mathbf{s}, t) &= \alpha_1 + z_{11}(\mathbf{s}) + z_{21}(t) \\ \eta_2(\mathbf{s}, t) &= \alpha_2 + z_{12}(\mathbf{s}) + z_{22}(t)\end{aligned}\tag{ii}$$

$$\begin{aligned}\eta_1(\mathbf{s}, t) &= \alpha_1 + z_{31}(\mathbf{s}, t) \\ \eta_2(\mathbf{s}, t) &= \alpha_2 + z_{32}(\mathbf{s}, t)\end{aligned}\tag{iii}$$

where $z_{1i}(\mathbf{s})$ is the realisation at location \mathbf{s} of the spatial process \mathbf{z}_{1i} with Matérn covariance function $\mathbf{z}_{1i} \sim MVN(\mathbf{0}, \sigma_{z_{1i}}^2 \boldsymbol{\Sigma})$, $z_{2i}(t) \sim N(z_{2i}(t-1), \sigma_{z_{2i}}^2)$ is a temporal process modelled as a random walk and $\mathbf{z}_{3i} \sim MVN(\mathbf{0}, \sigma_{z_{3i}}^2 \boldsymbol{\Sigma}_t \otimes \boldsymbol{\Sigma}_s)$ is a separable space-time interaction with Matérn covariance function and temporal dependence modelled as a random walk.

Based on the deviance information criterion (DIC), the results show that AQUM spatial variation is relevant but there is no need for a space-time interaction so model (ii) is selected for AQUM, while the PCM temporal variation is negligible so model (i) is selected for PCM (see Appendix B for details). Hence, we will use this specification in the joint model presented in the next section.

3.2 Bayesian joint spatio-temporal model for misaligned covariates

Following Kifle *et al.* (2017) we implement an additive space-time model for data observed at different points in space, which share a spatial and a temporal component.

Previous similar applications consider measurements of more than one variable at the same locations, but this is not a requirement in the INLA-SPDE approach.

Our model is joint in the sense that we specify one likelihood for the response and one for each of the misaligned covariates, and they contain common components which are estimated using all the data. Even though in R-INLA the problem is computationally treated similarly to a multivariate situation, this is not our case as we ultimately consider solely the monitor observations as response variable.

We make the assumption that the same temporal dynamics govern AQUM and monitor observations, and likewise the same spatial dynamics govern PCM, AQUM and monitor observations.

Our hierarchical model has three levels: in the first we define the likelihoods, in the second the random effect components, while the third level includes the prior distributions for the model parameters and hyperparameters.

The joint model presented below is implemented via INLA, a computationally efficient alternative to Markov chain Monte Carlo (MCMC) methods that works specifically on hierarchical Gaussian Markov Random Fields (GMRF). Details on how this is done in R-INLA can be found in Appendix E.

3.2.1 Level 1: Likelihoods and linear predictors

Let $y_i(\mathbf{s}, t)$ denote the PCM ($i = 1$) and AQUM ($i = 2$) data and the observed NO_2 concentration ($i = 3$) at the generic time point t and site \mathbf{s} , on the logarithmic scale. These are assumed to be normally distributed, with mean $\eta_i(\mathbf{s}, t)$ and measurement error variance $\sigma_{\epsilon_i}^2$:

$$y_1(\mathbf{s}, t) \sim N(\eta_1(\mathbf{s}), \sigma_{\epsilon_1}^2) \quad (\text{PCM})$$

$$y_2(\mathbf{s}, t) \sim N(\eta_2(\mathbf{s}, t), \sigma_{\epsilon_2}^2) \quad (\text{AQUM})$$

$$y_3(\mathbf{s}, t) \sim N(\eta_3(\mathbf{s}, t), \sigma_{\epsilon_3}^2) \quad (\text{Ground observations})$$

Based on the results from section 3.1 we model the PCM data with an intercept and a spatial component and the AQUM data with an intercept and additive spatial and temporal components. These are shared between the three linear predictors, which are the following:

$$\eta_1(\mathbf{s}) = \alpha_1 + z_1(\mathbf{s})\tag{1}$$

$$\eta_2(\mathbf{s}, t) = \alpha_2 + \lambda_{1,2} z_1(\mathbf{s}) + z_2(t)\tag{2}$$

$$\eta_3(\mathbf{s}, t) = \alpha_3 + \beta_{k_s} + \lambda_{1,3}z_1(\mathbf{s}) + \lambda_{2,3}z_2(t) + z_3(t, k_s) \quad (3)$$

where α_i are the intercepts, $\lambda_{i,j}$ are the scaling parameters for the shared components from η_i to η_j , β_{k_s} is the fixed effect for the site type as categorical variable ($k_s = 0$: rural (reference), $k_s = 1$: urban and $k_s = 2$: road-kerb side), and z_1 and z_2 are the shared random effects. The linear predictor for the ground observations η_3 also contains an interaction term z_3 which allows for a different residual temporal trend for each site type.

Note that even though PCM is assumed to be governed only by a spatial effect, its output does vary in both space and time, so the deterministic model output \mathbf{y}_1 has space and time indices (here the locations are the centroids of the 44117 PCM grid cell, and the time points are the years), while its latent field z_1 has only a spatial index.

For AQUM, the space and time indices of \mathbf{y}_2 correspond to the centroids of the 495 AQUM grid cell and the 1826 days respectively.

Finally, \mathbf{y}_3 is measured at the 126 monitors on 1826 days.

3.2.2 Level 2: latent fields

In Equation (3), $z_1 \sim MVN(\mathbf{0}, \sigma_{z_1}^2 \Sigma)$ is the common spatial latent field, with Σ being the correlation matrix defined by the Matérn stationary and isotropic covariance function (see Appendix D). It is important to note that z_1 is then rescaled for AQUM and monitor observations through $\lambda_{1,2}$ (eq. 2) and $\lambda_{1,3}$ (eq. 3).

In the same equation, $z_2(t)$ is the t -th element of the temporal latent field z_2 , and is modelled as a random walk: $z_2(t) \sim N(z_2(t-1), \sigma_{z_2}^2)$. Similarly to z_1 , z_2 is rescaled for the monitor observations through $\lambda_{2,3}$ (eq. 3).

Finally, z_3 is the residual temporal trend assumed to be different for each site type (rural, urban, road-kerb side), and modelled as first order autoregressive $z_3(t, k_s) \sim N(\rho z_3(t-1, k_s), \sigma_{z_3}^2)$. In other words, we assume conditionally independent replications of the same latent field for each site type, with shared hyperparameters (Martins *et al.*, 2013).

3.2.3 Level 3: priors

The priors on the model parameters are specified as follows.

According to Fuglstad *et al.* (2019), we choose a penalised complexity prior (Simpson *et al.*, 2017) for range and variance of the latent spatial field z_1 such that $P(r < r_0) = 0.95$ and $P(\sigma_{z_1} > \sigma_0) = 0.5$, where $r_0 = 1/5$ of the domain size and $\sigma_0 = 100$ (see Appendix D).

For the standard deviation of the random walk we assume a penalised complexity prior such that the probability that σ_{z_2} is greater than the empirical standard deviation of the AQUM data is 1%, i.e. $P(\sigma_{z_2} > SD(AQUM)) = 0.01$.

For the time-sitetype interaction we assume the default vague prior defined on the log-precision: $\log(1/\sigma_{z_3}^2) \sim \log\text{Gamma}(1, 5e-05)$; for the autoregressive parameter we assume $\rho \sim N(0.3, 0.5)$ using information from previous modelling exercise.

The precisions of response variable, AQUM data and PCM data are assigned the default vague prior $\log(1/\sigma_{\epsilon_i}^2) \sim \log\text{Gamma}(1, 5e-05)$, $i = 1, 2, 3$.

On the scaling coefficients we put a Normal prior centred on a positive values around 1 with a large variance to ensure minimal information: $\lambda_{1,2} \sim N(1.1, 100)$, $\lambda_{1,3} \sim N(1.3, 100)$, $\lambda_{2,3} \sim N(0.9, 100)$.

Finally on the coefficients of the fixed effects α_i and β_{k_s} we assume the default weak Normal prior distribution $N(0, 1000)$.

3.3 Competitor models

We compared our model to three different competitors: (i) a joint model that includes only one misaligned covariate (either AQUM or PCM), (ii) a simple hierarchical model that includes a covariate aligned at the monitoring sites through bilinear interpolation (Akima, 1978) or kriging, and (iii) a complex hierarchical model which allows for non-stationarity after interpolating the misaligned covariates via bilinear interpolation (Mukhopadhyay and Sahu, 2017).

The aim of this comparison is to evaluate if the inclusion of more than one extra data source actually improves the model predictive capability and can counterbalance the need for complex random effect structures, and if there is a gain in moving from a simple interpolation to a modelling framework.

We describe the three comparators in the rest of this section.

3.3.1 Joint models with one misaligned covariate only

The joint model that includes PCM only is specified as follows:

$$y_1(\mathbf{s}, t) \sim N(\eta_1(\mathbf{s}), \sigma_{\epsilon_1}^2) \quad (\text{PCM})$$

and

$$y_2(\mathbf{s}, t) \sim N(\eta_2(\mathbf{s}, t), \sigma_{\epsilon_2}^2) \quad (\text{Ground observations})$$

with

$$\eta_1(\mathbf{s}) = \alpha_1 + z_1(\mathbf{s}) \quad (\text{PCM})$$

$$\eta_2(\mathbf{s}, t) = \alpha_2 + \beta_{k_s} + \lambda_{1,2}z_1(\mathbf{s}) + z_3(t, k_s) \quad (\text{Ground observations})$$

Similarly, the joint model that includes AQUM only is defined as:

$$y_1(\mathbf{s}, t) \sim N(\eta_1(\mathbf{s}, t), \sigma_{\epsilon_1}^2) \quad (\text{AQUM})$$

and

$$y_2(\mathbf{s}, t) \sim N(\eta_2(\mathbf{s}, t), \sigma_{\epsilon_2}^2) \quad (\text{Ground observations})$$

with

$$\eta_1(\mathbf{s}, t) = \alpha_1 + z_1(\mathbf{s}) + z_2(t) \quad (\text{AQUM})$$

$$\eta_2(\mathbf{s}, t) = \alpha_2 + \beta_{k_s} + \lambda_{1,2}z_1(\mathbf{s}) + \lambda_{2,2}z_2(t) + z_3(t, k_s) \quad (\text{Ground observations})$$

For these models we considered either fixed to 1 or varying calibration coefficients $\lambda_{i,j}$, and different priors. The final choice of priors is the one reported in Section 3.2.3.

3.3.2 Data integration model via interpolation

We implement two models that use interpolation techniques to obtain values of AQUM and PCM at the monitoring stations. The first is a naive bilinear interpolation, the second can be considered as Bayesian kriging, as we predict AQUM and PCM at the monitoring stations from the models described in section 3.1.

In both cases, after aligning the AQUM (\mathbf{X}_1) and PCM (\mathbf{X}_2) values, we consider a linear effect on the covariates, a spatially structured residual z_1 , a temporally structured residual z_2 and the site-type-specific temporal effect z_3 specified as in Section 3.2. We also keep the fixed effects for the site type β_{k_s} as in the joint model.

We specify a normal likelihood $y(\mathbf{s}, t) \sim N(\eta(\mathbf{s}, t), \sigma_\epsilon^2)$ and the linear predictor as follows:

$$\eta(\mathbf{s}, t) = \beta_0 + \beta_1 X_1(\mathbf{s}, t) + \beta_2 X_2(\mathbf{s}, t) + \beta_{k_s} + z_1(\mathbf{s}) + z_2(t) + z_3(t, k_s)$$

3.3.3 Data integration model with non-stationarity

Mukhopadhyay and Sahu (2017) developed a site-type-specific regression on the AQUM data using our same classification for the site type. The key feature of their model is the specification of a non-stationary spatio-temporal process, which leads to a better predictive performance compared to the stationary Gaussian process (GP) in their application.

To obtain a like-for-like comparison, we also include a site-type-specific regression on the PCM data and implement both the stationary and the non-stationary versions of this model.

Both AQUM (\mathbf{X}_1) and PCM (\mathbf{X}_2) are interpolated at the monitoring site locations through bilinear interpolation.

The hierarchical model specification in this case is:

$$y(\mathbf{s}, t) \sim N(\eta(\mathbf{s}, t), \sigma_\epsilon^2)$$

$$\eta(\mathbf{s}, t) = \mu(\mathbf{s}, t) + \nu(\mathbf{s}, t)$$

with

$$\mu(\mathbf{s}, t) = \gamma_0 + \gamma_1 X_1(\mathbf{s}, t) + \sum_{k=1}^2 \delta_k(\mathbf{s})(\gamma_{0k} + \gamma_{1k} X_1(\mathbf{s}, t))$$

for the model with AQUM only, and

$$\mu(\mathbf{s}, t) = \gamma_0 + \gamma_1 X_1(\mathbf{s}, t) + \gamma_2 X_2(\mathbf{s}, t) + \sum_{k=1}^2 \delta_k(\mathbf{s})(\gamma_{0k} + \gamma_{1k} X_1(\mathbf{s}, t) + \gamma_{2k} X_2(\mathbf{s}, t))$$

for the model with AQUM and PCM.

Here $k = 0$ indicates rural site type (baseline), $k = 1$ urban and $k = 2$ road-kerbside, $\delta_k(s)$ is an indicator function equal to 1 if site s is of type k and 0 otherwise, γ_0 , γ_1 and γ_2 are the baseline intercept and slopes for \mathbf{X}_1 and \mathbf{X}_2 , while γ_{0k} , γ_{1k} and γ_{2k} are site-type-specific adjustments to the baseline intercept and slopes.

For the spatio-temporal process ν we first assume a stationary time-independent GP with zero mean and exponential correlation function (note that $\nu_t(s) = \nu(s, t)$):

$$\nu_t \sim N(\mathbf{0}, \sigma_\nu^2 \mathbf{H}_\nu(\phi)), \text{ where } \mathbf{H}_\nu(\phi) = \text{corr}(\nu_t(s), \nu_t(s')) = \exp(-\|s - s'\|/\phi).$$

Then we specify a non-stationary covariance structure as in Sahu and Mukhopadhyay (2015): given a GP ν_t^* defined on a set of $m = 25$ knot locations $\nu_t^* \sim MVN(\mathbf{0}, \sigma_{\nu^*}^2 \mathbf{H}_{\nu^*}(\phi))$, the Gaussian predictive process (GPP) at a new location s is defined as $\tilde{\nu}_t(s) = E[\nu_t(s)|\nu_t^*]$. From multivariate Gaussian theory it follows that $\tilde{\nu}_t = C^* \mathbf{H}_{\nu^*}^{-1}(\phi) \nu_t^*$ with C^* being the cross-correlation function between ν_t and ν_t^* .

The non-stationarity and the anisotropy are given by the fact that $\text{corr}(\tilde{\nu}_t(s), \tilde{\nu}_t(s')) = \mathbf{c}^*(s)^T \mathbf{H}_{\nu^*}^{-1}(\phi) \mathbf{c}^*(s')$ which depends on both s and s' and not only on the separation vector or the distance between locations.

To introduce temporal dependence we specify a first order autoregressive model for ν_t^* .

The choice of knot locations, model specification and prior distributions is based on Mukhopadhyay and Sahu (2017). This is justified by the fact that we use the same data sources on a subregion of their study area.

3.4 Validation and predictive capability measures

We compared the predictive capability through proper scoring rules (Gneiting and Raftery, 2007) such as the cross-validated logarithmic score (logScore), the Continuous Ranked Probability Score (CRPS) and the Root Mean Squared Error (RMSE), and also the Predictive Model Choice Criterion (PMCC) proposed by Gelfand and Ghosh (1998).

Furthermore, we reported the correlation between the observed and the predicted values for the validation sites (COR), the Mean Absolute Percentage Error (MAPE), and the 95% coverage (COV), defined as the percentage of times that the observed value falls within the 95% credibility interval of the sampled posterior marginal.

To measure the predictive capability we need to report the fitted values at the validation sites on the scale of the outcome, as cannot compare the observed values with the fitted values because they are not accounting for the measurement error, but only for the uncertainty associated with the model parameters. In order to do so, we draw 50 values from the marginal posterior of the measurement error $p(\sigma_{\epsilon_3}^2 | \mathbf{y}_3)$ first, then draw η_3 from its conditional posterior $p(\eta_3 | \sigma_{\epsilon_3}^2, \mathbf{y}_3)$ using the simulated values of $\sigma_{\epsilon_3}^2$ (Gelman *et al.*, 2013). These values are used as mean and variance of a Normal distribution, from which we sampled values at each site (sample size = 100).

The following are the formulas for the different measures of predictive capability used in the paper. For simplicity we apply a slight change of notation here: y_{jt} indicates the observed value at monitor j (m is the number of validation monitors) and day t ($t = 1, \dots, T, T=1826$), and \hat{y}_{jt} is the corresponding predicted value obtained as mean of the vector of $Q = 100 \times 50$ sampled values $\hat{\mathbf{y}}_{jt} = \hat{y}_1, \dots, \hat{y}_Q \sim F_{jt}$, F_{jt} being the empirical distribution function of $\hat{\mathbf{y}}_{jt}$.

$$\begin{aligned} RMSE &= \sqrt{\frac{1}{mT} \sum_{j=1}^m \sum_{t=1}^T (y_{jt} - \hat{y}_{jt})^2} \\ MAPE &= \frac{1}{mT} \sum_{j=1}^m \sum_{t=1}^T \frac{|y_{jt} - \hat{y}_{jt}|}{y_{jt}} \cdot 100 \\ PMCC &= \sum_{j=1}^m \sum_{t=1}^T (y_{jt} - \hat{y}_{jt})^2 + \sum_{j=1}^m \sum_{t=1}^T \text{VAR}(\hat{\mathbf{y}}_{jt}) \\ CRPS &= \frac{1}{mT} \sum_{j=1}^m \sum_{t=1}^T CRPS(F_{jt}, y_{jt}) \quad , \text{ with} \\ CRPS(F_{jt}, y_{jt}) &= \frac{1}{Q} \sum_{q=1}^Q |\hat{y}_q - y_{jt}| - \frac{1}{2Q^2} \sum_{q=1}^Q \sum_{r=1}^Q |\hat{y}_q - \hat{y}_r| \end{aligned}$$

For each model under comparison, the predictive capability measures presented above are computed pooling together the 6 validation sets. It can be calculated by day, by site, by site type or across all sites to obtain specific and global measures, with lowest measures indicating the best predictive performance.

3.5 Predictions on a regular grid

From the joint model, we extract daily predictions of NO_2 concentration on a regular grid that covers the study area. For the grid we choose an intermediate spatial resolution between PCM and AQUM data to limit the computational burden while retaining spatial variability.

In order to provide the predictions in a reasonable time, we extract samples from the joint posterior marginals and estimate the linear predictor at each time-location for the 1826 days on the regular grid (Thomas *et al.*, 2019).

We compute the predictions from the model that includes all monitors as training set.

We extract samples from the posterior marginals of the model components in order to reconstruct the linear predictor at each time-location for the 1826 days on the regular grid, as:

$$\eta_3(\mathbf{s}, t) = \alpha_3 + \beta_{k_s} + \lambda_{1,3}z_1(\mathbf{s}) + \lambda_{2,3}z_2(t) + z_3(t, k_s)$$

In particular, following the tutorial by Bakka (2017), we obtain samples from the posterior of the intercept α_3 and β_{k_s} for each site type, samples from the posterior of $\lambda_{1,3}z_1$ at the mesh nodes and reproject it on the prediction grid, samples from the posterior of $\lambda_{2,3}z_2$ at each time point (days), and samples from the posterior of z_3 for each day and site type.

Note that in order to predict at the grid locations we need to know the value of site type classification for each grid point. With this aim we built a function which assigns each location to road-kerb side, urban or rural depending on the distance from any road as well as using the Corine land cover for the year 2012 for the UK, Jersey and Guernsey shapefile from the Centre for Ecology and Hydrology (Cole *et al.*, 2015). See Appendix F for more details.

For each sample we then sum up the samples from the fixed effects and random effects to reconstruct the linear predictor, then the prediction is given by average across all samples.

4 Results

In this section we present the results of the model comparison, with particular focus on the advantages of the proposed joint model, and the daily predictions that we obtained from the best model.

4.1 Model comparison

In order to show whether the inclusion of more than one extra data source actually improves the model predictive capability, we compare our proposed joint model with the corresponding models that include only AQUM or PCM.

For AQUM we assume a spatio-temporal effect or temporal-only effect when PCM is included.

We also compare our joint model with other well established data integration techniques, the simple interpolation models described in section 3.3.2 and the more complex ones described in section 3.3.3.

Besides providing information about all the sources of uncertainty, all the joint models have better performance than the models where the misaligned data are interpolated, even allowing for non-stationarity (see table 2).

However, the AQUM data do not seem to provide much information, in fact the model that includes only AQUM has a far worse performance than the one only including PCM. In addition, allowing for a spatial effect on AQUM does not improve the prediction, for the model where PCM is also included. This can be explained by the fact that the time-sitetype interaction z_3 replaces the role of AQUM in capturing the temporal trend when we remove AQUM from the model and the temporal information is still provided by the numerous monitoring stations, while there is no other structured spatial component that compensates for PCM when it is removed.

Furthermore, as we focus here on spatial prediction rather than temporal forecasting, removing AQUM is less of a burden on the model performance in terms of predictive capability.

Nevertheless the model including both AQUM and PCM has the best performance in terms of PMCC and CRPS and we will report the results from this model in the next section.

Note that the predictive capability measures of the models in section 3.3.3 cannot be compared with the others due to the different model structure. Only the PMCC and the 95% coverage are comparable and reported in table 2.

Table 2: Model comparison in terms of predictive capability

Model**	Predictive capability					
	PMCC	CRPS	RMSE	MAPE	CORR	COV
$AQUM(s, t)$ joint	18277	0.0523	0.5725	16.71%	65.83%	78.15%
$PCM(s)$ joint	14018	0.0372	0.4615	13.54%	76.77%	86.87%
$AQUM(s, t) + PCM(s)$ joint	13621	0.0338	0.4665	13.67%	76.08%	84.66%
$AQUM + PCM$ bilinear interpolation	82970	0.2560	0.6911	17.57%	67.14%	68.55%
$AQUM + PCM$ kriging estimates	35017	0.2220	0.4964	14.58%	73.13%	75.27%
$AQUM$, non-stationary (Mukhopadhyay and Sahu, 2017)	79542*					60.74%
$AQUM + PCM$, non-stationary (Mukhopadhyay and Sahu, 2017)	75506*					62.13%
$AQUM + PCM$, stationary (Mukhopadhyay and Sahu, 2017)	75510*					62.13%

* As provided by spT.Gibbs function in R package spAir.

** (s) indicates spatial-only random effects; (t) indicates temporal-only random effects; (s, t) indicates additive spatial and temporal random effects. When not specified, a linear effect is assumed as described in section 3.3.

Table 3: Summary of model parameters and hyperparameters

	mean	SD	0.025q	median	0.975q
α_1	2.0653	0.0308	2.0048	2.0653	2.1258
α_2	2.5793	0.0259	2.5285	2.5793	2.6301
α_3	2.4722	0.0236	2.4258	2.4722	2.5186
β_{URB}	-0.1716	0.0047	-0.1808	-0.1716	-0.1624
β_{RKS}	0.3764	0.0047	0.3673	0.3764	0.3856
$\sigma_{\epsilon_1}^2$	0.0003	0.0000	0.0003	0.0003	0.0003
$\sigma_{\epsilon_2}^2$	0.0303	0.0000	0.0303	0.0303	0.0303
$\sigma_{\epsilon_3}^2$	0.0213	0.0000	0.0213	0.0213	0.0213
$\sigma_{z_1}^2$	2.0729	0.0385	1.9815	2.0803	2.1225
$\sigma_{z_2}^2$	2626.3	7.960	2607.8	2627.7	2637.7
$\sigma_{z_3}^2$	0.0013	0.0000	0.0013	0.0013	0.0013
r_{z_1} (km)	177.8	0.227	177.2	177.77	256.0
ρ_{z_3}	0.5702	0.0005	0.5689	0.5700	0.6869
$\lambda_{1,2}$	1.1000	0.0001	1.0996	1.0999	1.1345
$\lambda_{1,3}$	1.2999	0.0003	1.2989	1.2998	1.3990
$\lambda_{2,3}$	0.8995	0.0004	0.8977	0.8995	0.9003

With regard to these models, allowing for non-stationarity and anisotropy leads to very little gain compared to the introduction of an additional source of data at high spatial resolution. In general, their performance is almost as poor as having a linear effect on interpolated covariates.

4.2 Results from the complete joint model

We report the results for the joint model that includes spatial and temporal effects on AQUM and spatial effect on PCM, re-ran using all monitors as training data.

Looking at the summary reported in table 3 we see that, as expected, there is an increase in the NO_2 concentration going from rural to road-kerb side locations, but not for urban. For the spatial latent field z_1 , the estimated empirical range, i.e. the distance after which the spatial correlation function drops to 0.13 (Lindgren and Rue, 2015), is 177 Km, corresponding to approximately 50% of the maximum extension of the spatial domain.

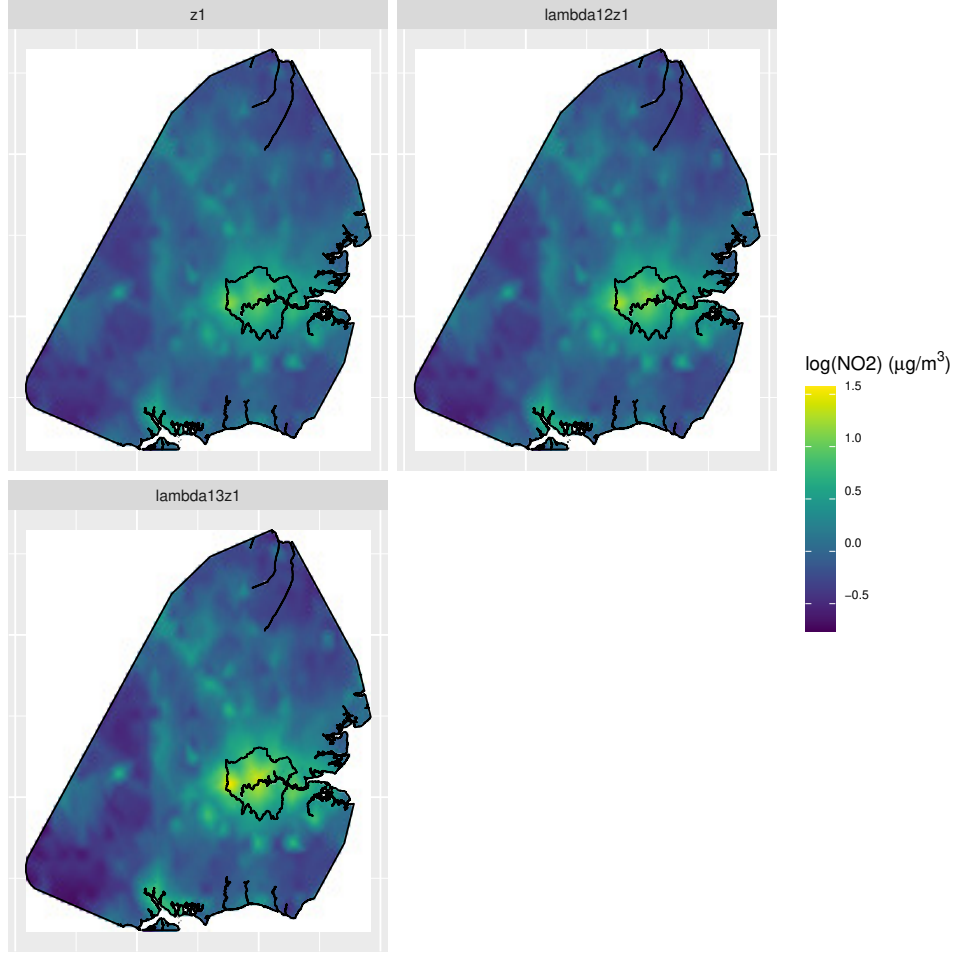


Figure 2: Posterior mean of the latent spatial field z_1 and of the rescaled spatial fields $\lambda_{1,2}z_1$ and $\lambda_{1,3}z_1$.

The scaling parameters $\lambda_{i,j}$ are all different from 1, meaning the spatial field for PCM needs to be rescaled for AQUM ($\lambda_{1,2} = 1.1$) and for the monitor observations ($\lambda_{1,3} = 1.3$), and the temporal latent field for AQUM is also calibrated against the monitor observations with $\lambda_{2,3} = 0.9$.

The intercepts α_i represent the overall mean of PCM, AQUM and ground observations respectively.

The spatial latent field z_1 (Fig. 2) shared between the PCM data, the AQUM data and the monitor observations shows the traffic-driven characteristics of NO_2 as we can recognize higher values in correspondence of motorways and major city centers. The rescaled fields are reported as well and for $\lambda_{1,3}z_1$ the magnifying effect of the scaling parameter $\lambda_{1,3} = 1.3$ is particularly visible.

Figure 3 shows the temporal latent field z_2 shared between the AQUM data and the monitor observations which captures the seasonality of NO_2 , and the rescaled field $\lambda_{2,3}z_2$ which is shrunk by the scaling parameter $\lambda_{2,3} = 0.9$.

The latent fields z_1 and z_2 are both centred in zero as the large scale component of PCM and AQUM is captured by their intercepts α_1 and α_2 .

Finally, the time-sitetype interaction z_3 in Fig. 4 shows that there is some residual site-type-specific temporal variability, especially for urban and road-kerb side monitors, which is not captured by the main temporal component z_2 .

4.2.1 Daily predictions

We selected four NO_2 pollution episodes reported by the LondonAir website (King's College London, 2018) and compared the predictions for these four days with four randomly selected summer Sundays across the study period,

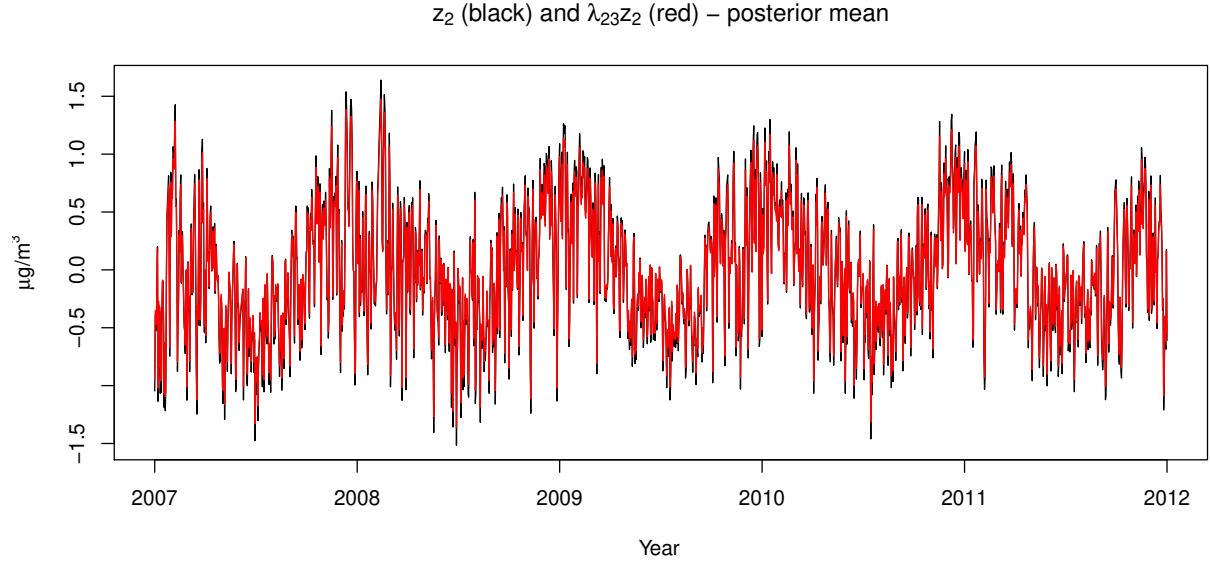


Figure 3: Posterior mean of the latent temporal field z_2 (black line) and of the rescaled temporal field $\lambda_{2,3}z_2$ (red line).

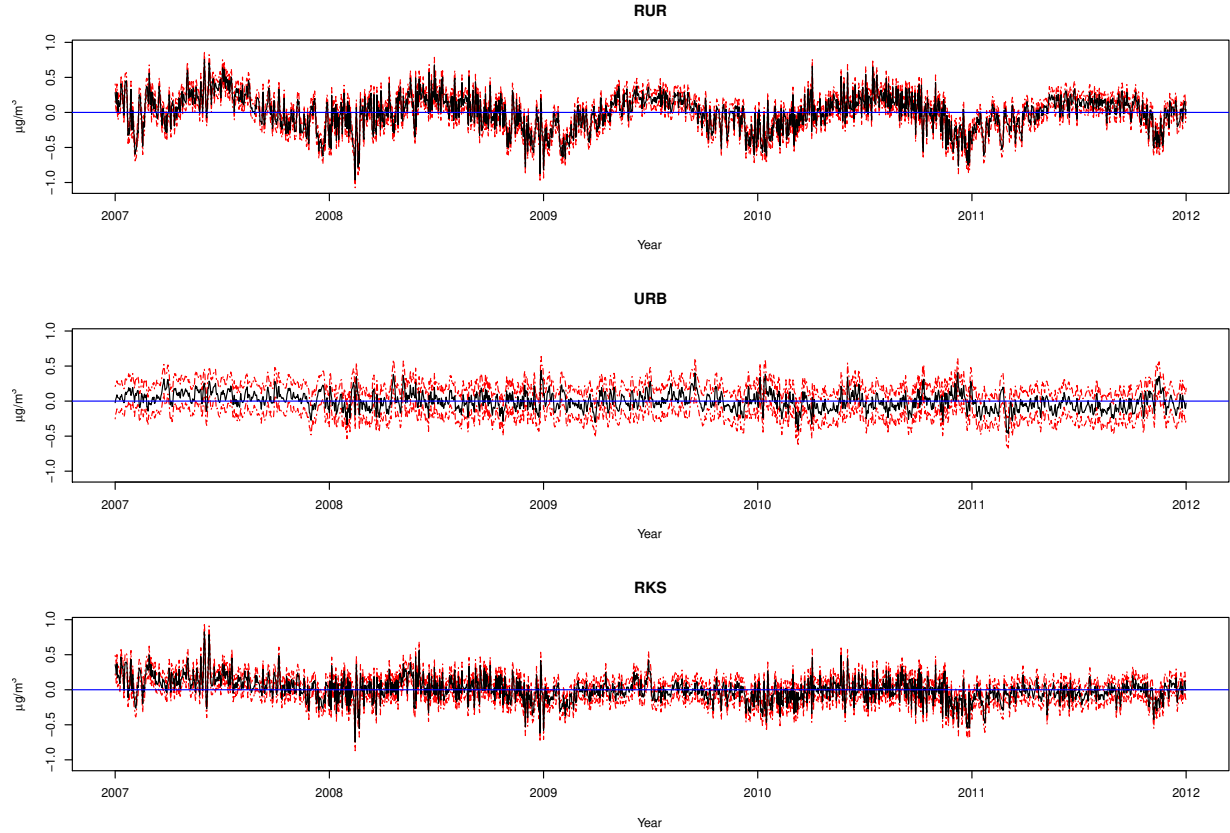


Figure 4: Time-sitetype interaction z_3 . Posterior mean in red, 95% CI in black dashed lines.

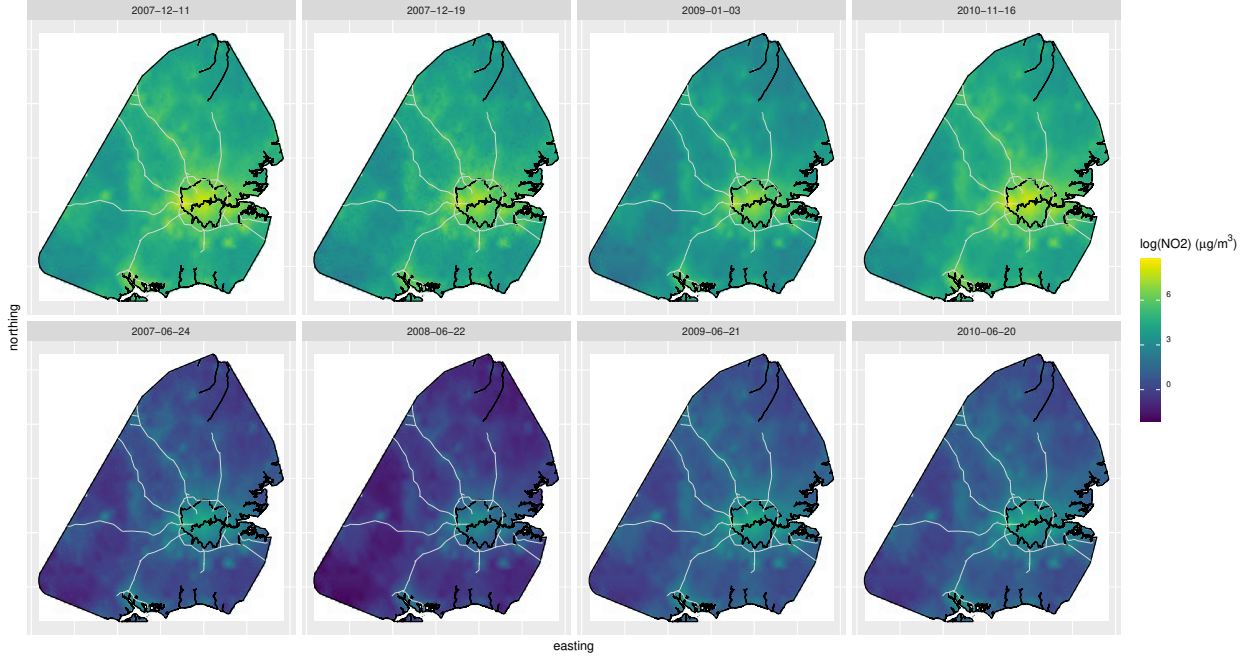


Figure 5: Daily predictions for four days in which an air pollution event was registered (top row) and four days with reported low air pollution concentration (bottom row).

where we expect to see low levels of NO_2 . The predictions show the expected behaviour, with high predicted concentrations during the pollution episodes and low concentrations during the selected Sundays (Fig. 5).

A layer with the roads classified as motorways is plotted on top of each map, showing correspondence between the highest predicted levels of NO_2 and the major roads. This is expected because NO_2 is a highly traffic-driven pollutant. A peak of NO_2 concentration can also be observed in the area of Heathrow airport, on the left of Greater London, which is characterised by the highest levels also on low concentration days.

5 Conclusion and discussion

We implemented a hierarchical Bayesian model to estimate air pollution concentration, combining misaligned data sources with a joint approach. This approach can be considered in between Bayesian melding and calibration, and it is the first attempt at implementing such methods on spatio-temporal air pollution data in R-INLA.

The proposed model includes information on the site type as well as output from two different numerical models characterised by spatial and temporal variability and accounting for traffic, chemistry, land use and meteorological covariates. Our method is transferable to any available data sources, however the interpretation of the results may change according to their intrinsic characteristics, in particular referring to the information included in the deterministic or LUR models.

We show that including more than one covariate at different spatial and temporal resolution increases model predictive capability. However, removing AQUM has proven not to be detrimental, but this could be justified with the fact that we are not doing temporal forecasting.

Overall we prove that using as much spatial and temporal information as possible is more beneficial than increasing the complexity of the random effect structure.

A time-site type interaction was added to the model to account for residual temporal variability observed when looking at the site type-specific residuals.

The advantages of our method are manyfolds: first, reconstructing the entire latent field in a Bayesian approach provides us with the marginal posterior distribution for all the uncertainty parameters, allowing us to correctly quantify the uncertainty associated with our predictions and the deterministic models, that is not possible to obtain with other downscalers and non-model-based solutions; second, unlike the spatio-temporal downscaler proposed by Berrocal *et al.*

(2012), our model reconstructs the latent fields of the misaligned covariates as a whole, rather than locally. For the same reason, in order to obtain daily predictions at new locations there is no need to calculate the value of the misaligned covariates at the prediction locations, as the model already estimates the whole latent field.

Our analysis presents some limitations related on one side to the computational requirements of INLA due to the high number of parameters, and on the other side to the generalizability of the results, as the models are quite data-sensitive. In particular, we have very few rural sites even though we extended the study domain outside Greater London, suggesting the presence of preferential sampling that we did not account for. Furthermore, we made assumptions of stationarity and isotropy which may not hold when extending the spatial domain to bigger areas.

As a next step we will extend the joint model to a multivariate version including other pollutants, such as PM_{10} or O_3 .

In the future, the predicted air pollution concentration with associated measure of uncertainty could be used as exposure in an epidemiological model, allowing for uncertainty propagation.

Acknowledgements

The authors wish to thank the King’s College London Environmental Research Group and Paul Agnew from the Met Office for providing the data, Ben Barratt (King’s College London) and Monica Pirani (Imperial College London) for the valuable comments, and Haakon Bakka for the priceless explanations on INLA functions. This work was supported by the Medical Research Council [grant number MR/M025195/1]. Chiara Forlani was funded by Imperial College London President’s PhD scholarship. Michela Cameletti has been supported by the PRIN EphaStat Project (Project No. 20154X8K23, <https://sites.google.com/site/ephastat/>) provided by the Italian Ministry for Education, University and Research.

References

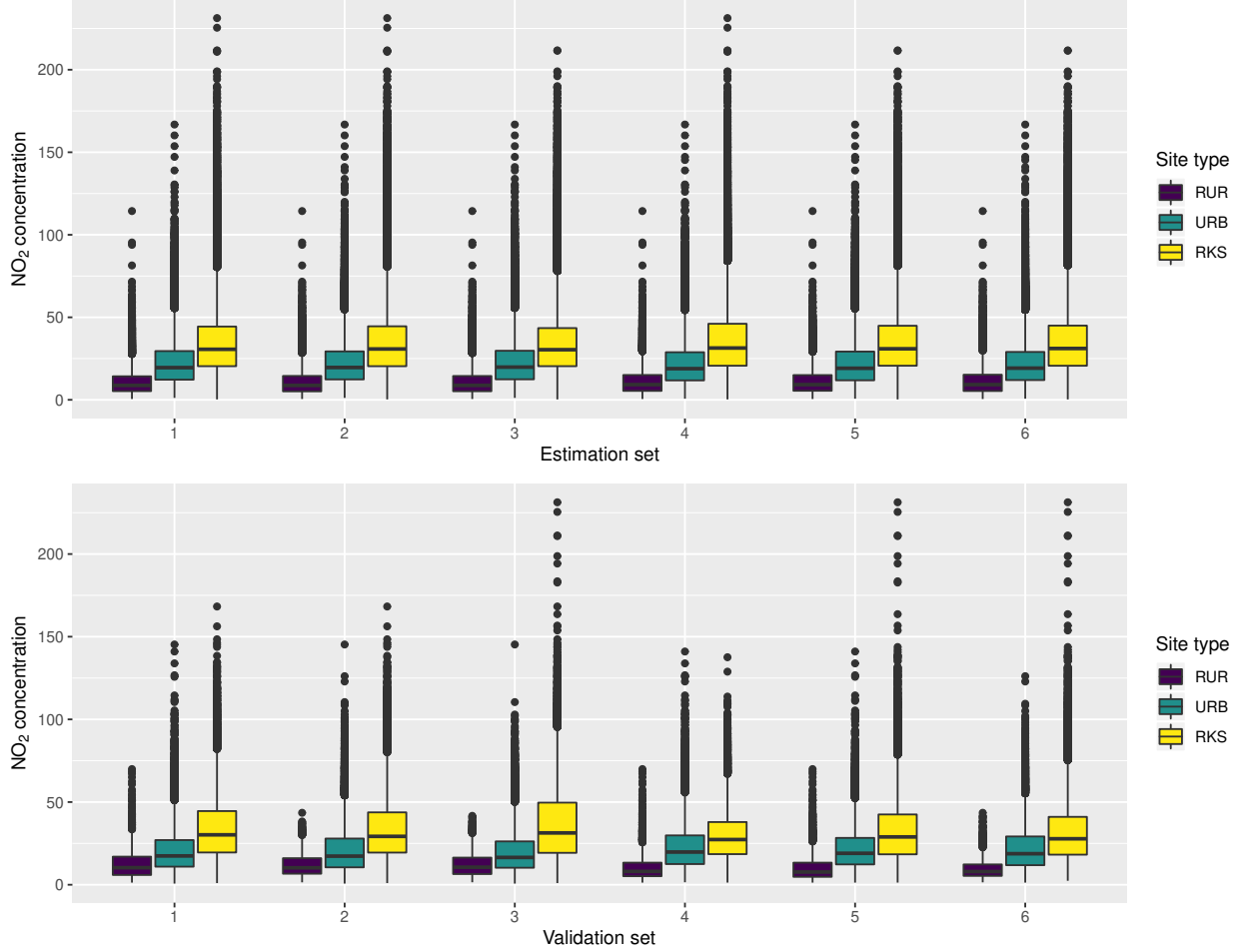
- Akima H, 1978. A Method of Bivariate Interpolation and Smooth Surface Fitting for Irregularly Distributed Data Points. *ACM Transactions on Mathematical Software* **4**(2): 148–159.
- Atkinson RW, Mills IC, Walton HA, Anderson HR, 2015. Fine particle components and health—a systematic review and meta-analysis of epidemiological time series studies of daily mortality and hospital admissions. *Journal of Exposure Science and Environmental Epidemiology* **25**: 208–214.
- Bakka H, 2017. Predictions with iid effects - binomial example: Building up the samples model component by model component (https://haakonbakkagit.github.io/btopic112.html#64_alternative_way:_building_up_the_samples_model_component_by_model_component).
- Bakka H, 2018. How to solve the stochastic partial differential equation that gives a Matérn random field using the finite element method. *arXiv e-prints* (2): arXiv:1803.03765v2.
- Berrocal VJ, 2019. Data assimilation. In Gelfand AE, Fuentes M, Hoeting JA, Smith RL (eds.), *Handbook of Environmental and Ecological Statistics*, chapter 7, CRC Press, 854.
- Berrocal VJ, Gelfand AE, Holland DM, 2010. A spatio-temporal downscaler for output from numerical models. *Journal of Agricultural, Biological, and Environmental Statistics* **15**(2): 176–197.
- Berrocal VJ, Gelfand AE, Holland DM, 2012. Space-Time Data fusion Under Error in Computer Model Output: An Application to Modeling Air Quality. *Biometrics* **68**(3): 837–848.
- Blangiardo M, Cameletti M, 2015. *Spatial and Spatial-temporal Bayesian Models with R-INLA*. Wiley.
- Cameletti M, Gómez-Rubio V, Blangiardo M, 2019. Bayesian modelling for spatially misaligned health and air pollution data through the INLA-SPDE approach. *Spatial Statistics* **31**: 100353.
- Chang HH, 2016. Data Assimilation for Environmental Pollution Fields. In Lawson AB, Banerjee S, Haining RP, Ugarte MD (eds.), *Handbook of Spatial Epidemiology*, chapter 16, CRC Press, 289–302.
- Cole B, King S, Ogutu B, Palmer D, Smith G, Balzter H, 2015. Corine land cover 2012 for the UK, Jersey and Guernsey. COMEAP, 2015. Statement on the evidence for the effects of nitrogen dioxide on health. Technical report.
- DEFRA, 2018. Data archive (<https://uk-air.defra.gov.uk/data/>).
- DLR, 2016. Global Urban Footprint (https://www.dlr.de/eoc/en/desktopdefault.aspx/tabid-9628/16557_read-40454/).
- Dominici F, Peng RD, Barr CD, Bell ML, 2010. Protecting human health from air pollution: shifting from a single-pollutant to a multipollutant approach. *Epidemiology* **21**(2): 187–94.
- EPA, 2016. National Ambient Air Quality Standards (<https://www.epa.gov/criteria-air-pollutants/naaqs-table>).

- Esch T, Heldens W, Hirner A, Keil M, Marconcini M, Roth A, Zeidler J, Dech S, Strano E, 2017. Breaking new ground in mapping human settlements from space – The Global Urban Footprint. *ISPRS Journal of Photogrammetry and Remote Sensing* **134**(June): 30–42.
- European Commission, 2018. Air Quality Standards (<http://ec.europa.eu/environment/air/quality/standards.htm>).
- Fuglstad GA, Simpson DP, Lindgren FK, Rue H, 2019. Constructing Priors that Penalize the Complexity of Gaussian Random Fields. *Journal of the American Statistical Association* **114**(525): 445–452.
- Gelfand AE, Ghosh SK, 1998. Model choice: A minimum posterior predictive loss approach. *Biometrika* **85**(1): 1–11.
- Gelfand AE, Sahu SK, Holland DM, 2012. On the effect of preferential sampling in spatial prediction. *Environmetrics* **23**(7): 565–578.
- Gelman A, Carlin JB, Stern HS, Dunson DB, Vehtari A, Rubin DB, 2013. *Bayesian Data Analysis*. CRC Press, 3 edition, 675 pp.
- Gneiting T, Raftery AE, 2007. Strictly Proper Scoring Rules, Prediction, and Estimation. *Journal of the American Statistical Association* **102**(477): 359–378.
- Gómez-Rubio V, 2019. *Bayesian inference with INLA*.
- Hoek G, Beelen R, de Hoogh K, Vienneau D, Gulliver J, Fischer PH, Briggs DJ, 2008. A review of land-use regression models to assess spatial variation of outdoor air pollution.
- Huang G, Lee D, Scott E, 2017. Multivariate space-time modelling of multiple air pollutants and their health effects accounting for exposure uncertainty. *Statistics in Medicine* (November): 1–15.
- Huang G, Lee D, Scott M, 2015. An integrated Bayesian model for estimating the long-term health effects of air pollution by fusing modelled and measured pollution data: A case study of nitrogen dioxide concentrations in Scotland. *Spatial and Spatio-temporal Epidemiology* **14-15**: 63–74.
- Johnson M, Isakov V, Touma JS, Mukerjee S, Özkaynak H, 2010. Evaluation of land-use regression models used to predict air quality concentrations in an urban area. *Atmospheric Environment* **44**(30): 3660–3668.
- Keller JP, Peng RD, 2019. Error in estimating area-level air pollution exposures for epidemiology. *Environmetrics* **30**(8).
- Kifle YW, Hens N, Faes C, 2017. Cross-covariance functions for additive and coupled joint spatiotemporal SPDE models in R-INLA. *Environmental and Ecological Statistics* **24**(4): 551–586.
- King’s College London, 2018. London Air LAQN Monitoring Statistics (<http://www.londonair.org.uk>).
- King’s College London ERG, 2016. STEAM project (<https://www.kcl.ac.uk/lsm/research/divisions/aes/research/ERG/science-policy/STEAM-Project.aspx>).
- Krainski ET, Gómez-Rubio V, Bakka H, Lenzi A, Castro-Camilo D, Simpson DP, Lindgren FK, Rue H, 2018. *Advanced Spatial Modeling with Stochastic Partial Differential Equations Using R and INLA*. CRC Press, 300 pp.
- Lee D, Ferguson C, Marian Scott E, 2011. Constructing representative air quality indicators with measures of uncertainty. *Journal of the Royal Statistical Society. Series A: Statistics in Society* **174**(1): 109–126.
- Lee D, Mukhopadhyay S, Rushworth A, Sahu SK, 2017. A rigorous statistical framework for spatio-temporal pollution prediction and estimation of its long-term impact on health. *Biostatistics* **18**(2): 370–385.
- Lee D, Sarran C, 2015. Controlling for unmeasured confounding and spatial misalignment in long-term air pollution and health studies. *Environmetrics* **26**(7): 477–487.
- Lindgren FK, Rue H, 2015. Bayesian Spatial Modelling with R-INLA. *Journal of Statistical Software* **63**(19): 1–25.
- Lindgren FK, Rue H, Lindström J, 2011. An explicit link between gaussian fields and gaussian markov random fields: The stochastic partial differential equation approach. *Journal of the Royal Statistical Society. Series B (Methodological)* **73**(4): 423–498.
- Lipfert FW, 2017. A critical review of the ESCAPE project for estimating long-term health effects of air pollution. *Environment International* **99**: 87–96.
- Martins TG, Simpson DP, Lindgren FK, Rue H, 2013. Bayesian computing with INLA: New features. *Computational Statistics and Data Analysis* **67**: 68–83.
- McMillan NJ, Holland DM, Morara M, Feng J, 2010. Combining numerical model output and particulate data using Bayesian space–time modeling. *Environmetrics* **21**(1): 48–65.
- Met Office, 2018. Air Quality Unified Model (<http://www.metoffice.gov.uk/research/modelling-systems/unified-model>).

- Moraga P, Cramb SM, Mengersen KL, Pagano M, 2017. A geostatistical model for combined analysis of point-level and area-level data using INLA and SPDE. *Spatial Statistics* **21**: 27–41.
- Mukhopadhyay S, Sahu SK, 2017. A Bayesian spatiotemporal model to estimate long-term exposure to outdoor air pollution at coarser administrative geographies in England and Wales. *Journal of the Royal Statistical Society. Series A: Statistics in Society* **181**(2): 465–486.
- NASA LP DAAC, 2013. MODIS Land Cover Type Yearly L3 Global 500 m SIN Grid (https://lpdaac.usgs.gov/dataset_discovery/modis/modis_products_table/mcd12q1).
- Ordnance Survey, 2017. OS Open Roads (URL: <https://www.ordnancesurvey.co.uk/business-and-government/products/os-open-roads.html>).
- Pannullo F, Lee D, Waclawski E, Leyland AH, 2016. How robust are the estimated effects of air pollution on health? Accounting for model uncertainty using Bayesian model averaging. *Spatial and Spatio-temporal Epidemiology* **18**: 53–62.
- Raftery AE, Fuentes M, 2005. Model Evaluation and Spatial Interpolation by Bayesian Combination of Observations with Outputs from Numerical Models. *Source: Biometrics* **61**(March): 36–45.
- Ricardo Energy & Environment, 2017. Technical report on UK supplementary assessment under the Air Quality Directive (2008 / 50 / EC), the Air Quality Framework Directive (96 / 62 / EC) and Fourth Daughter Directive (2004/107/EC) for 2015. Technical Report 1, Ricardo Energy & Environment.
- Rue H, 2018. R-INLA webpage (<http://www.r-inla.org/>).
- Rue H, Riebler A, Sørbye SH, Illian JB, Simpson DP, Lindgren FK, 2017. Bayesian Computing with INLA: A Review. *Annual Review of Statistics and Its Application* **4**: 395–421.
- Sahu SK, Gelfand AE, Holland DM, 2010. Fusing point and areal level space-time data with application to wet deposition. *Journal of the Royal Statistical Society. Series C: Applied Statistics* **59**(1): 77–103.
- Sahu SK, Mukhopadhyay S, 2015. On generating a flexible class of anisotropic spatial models using Gaussian predictive processes. Technical Report May, University of Southampton.
- Savage NH, Agnew P, Davis LS, Ord Nez C, Thorpe R, Johnson CE, O ’connor FM, Dalvi M, 2013. Air quality modelling using the Met Office Unified Model (AQUUM OS24-26): model description and initial evaluation. *Geosci. Model Dev* **6**: 353–372.
- Schmidt AM, Gelfand AE, 2003. A Bayesian coregionalization approach for multivariate pollutant data. *Journal of Geophysical Research* **108**(D24): n/a–n/a.
- Shaddick G, Thomas ML, Green A, Brauer M, van Donkelaar A, Burnett R, Chang HH, Cohen A, Dingenen RV, Dora C, Gumy S, Liu Y, Martin RV, Waller LA, West J, Zidek JV, Prüss-Ustün A, 2017. Data integration model for air quality: A hierarchical approach to the global estimation of exposures to ambient air pollution. *Journal of the Royal Statistical Society. Series C: Applied Statistics* : 231–253.
- Shaddick G, Wakefield JC, 2002. Modelling multivariate pollutant data at multiple sites. *Applied Statistics* **51**(D1m): 351–372.
- Shaddick G, Zidek JV, Liu Y, 2015. Mitigating the effects of preferentially selected monitoring sites for environmental policy and health risk analysis. *Spatial and Spatio-temporal Epidemiology* **18**: 44–52.
- Simpson DP, Rue H, Riebler A, Martins TG, Sørbye SH, 2017. Penalising model component complexity: A principled, practical approach to constructing priors. *Journal of Statistical Science* **32**(1): 1–28.
- Thomas ML, Shaddick G, Simpson D, de Hoogh K, Zidek JV, 2019. Data integration for high-resolution, continental-scale estimation of air pollution concentrations. *arXiv e-prints* (2): arXiv:1907.00093v2.
- WHO, 2006. Air quality guidelines for particulate matter, ozone, nitrogen dioxide and sulfur dioxide Global update 2005. Technical report.
- Wikle CK, Berliner LM, 2005. Combining Information Across Spatial Scales. *Technometrics* **47**(1): 80–91.
- Zidek JV, Le ND, Liu Z, 2012. Combining data and simulated data for space-time fields: Application to ozone. *Environmental and Ecological Statistics* **19**(1): 37–56.

A Further figures

Additional figures mentioned in the paper are reported here.

Figure A.1: Boxplot of NO₂ concentration by site type for each estimation and validation set.

B Comparison of separate models for AQUM and PCM data

Table B.1 shows the deviance information criterion (DIC) and the logarithmic score for the models implemented separately for AQUM and PCM.

We need to include a spatial component for AQUM as this significantly improves the model performance.

According to the reported measures, the spatial-only model for PCM is the worst in terms of goodness of fit. However, the temporal component seems negligible and when including a space-time interaction the range becomes unreasonable (5230 Km). For these reasons, and to limit the computational burden, we decided to keep only the spatial component when modelling PCM, also because the temporal information is provided by the monitors and the AQUM data at a much higher resolution (daily instead of annual).

C INLA-SPDE

In this section we define the class of models on which we can perform Bayesian inference using INLA and briefly introduce how the inference is computed, following the notation in Blangiardo and Cameletti (2015).

Let us consider a set of data $\mathbf{y} = (y_1, \dots, y_n)$ with distribution characterized by a parameter $\boldsymbol{\mu}$, usually the mean, defined as a function of an additive linear predictor $g(\boldsymbol{\mu}) = \boldsymbol{\eta}$:

$$g(\mu_i) = \eta_i = \alpha + \sum_{m=1}^M \beta_m x_{mi} + \sum_{l=1}^L f_l(z_{li})$$

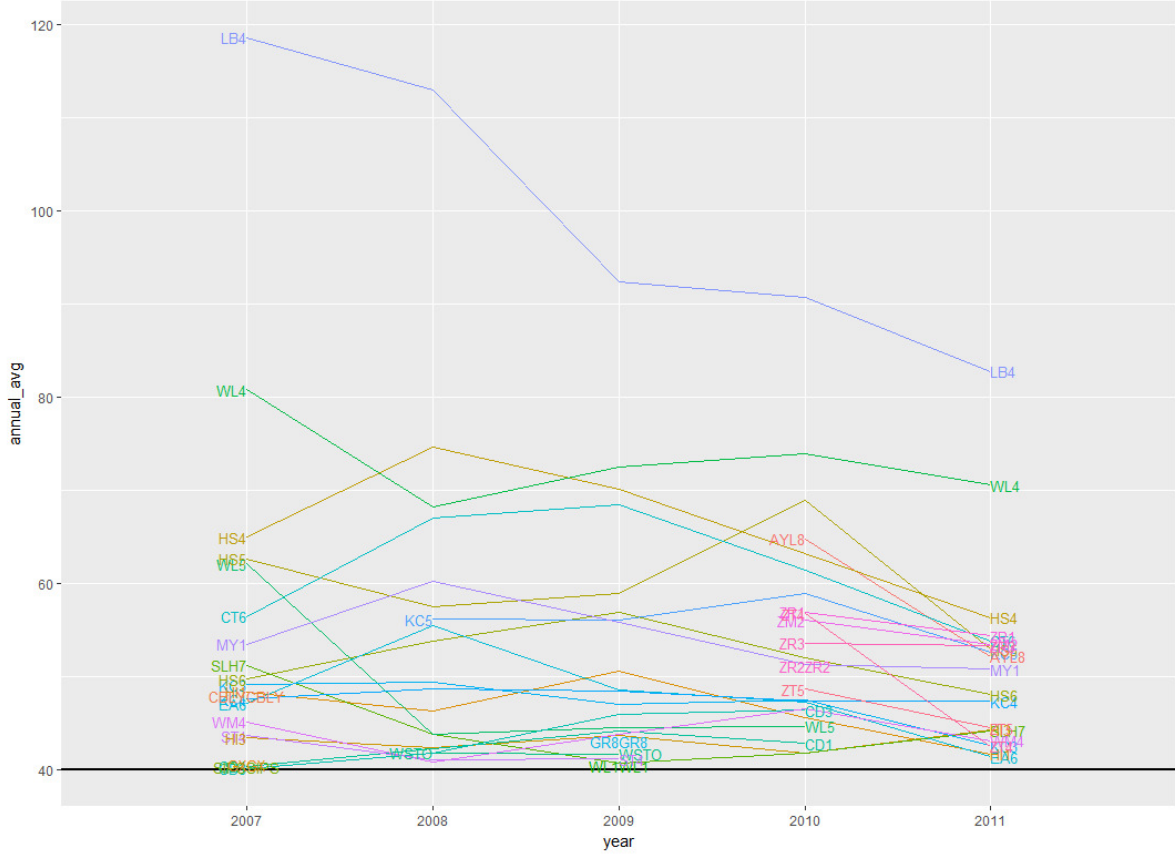


Figure A.2: Annual averages of NO₂ hourly concentration for monitoring sites that exceeded the WHO annual threshold of $40\mu\text{g}/\text{m}^3$ at least once in the study period.

Table B.1: Comparison of performance for separate models of AQUM and PCM

Model *	DIC	logScore
(i) $AQUM(t)$	1155407	0.64
(ii) $AQUM(s + t)$	659641	0.36
(iii) $AQUM(s * t)$	1418821	0.79
(i) $PCM(s)$	-373298	-0.85
(ii) $PCM(s + t)$	-403560	-0.91
(iii) $PCM(s * t)$	-456714	-1.04

* (t) indicates temporal-only random effect;
 (s) indicates spatial-only random effect;
 $(s + t)$ indicates additive spatial and temporal effects;
 $(s * t)$ indicates space-time interaction.

Defining the vector of parameters $\boldsymbol{\theta} = (\alpha, \beta, \mathbf{f})^T$ and the vector of hyperparameters $\boldsymbol{\psi} = (\psi_1, \dots, \psi_K)$, the likelihood is given by

$$p(\mathbf{y}|\boldsymbol{\theta}, \boldsymbol{\psi}) = \prod_{i=1}^n p(y_i|\theta_i, \boldsymbol{\psi})$$

We assume the latent field $\boldsymbol{\theta}$ to be multivariate Normal with precision matrix \mathbf{Q} and conditionally independent, i.e. a Gaussian Markov Random Field (GMRF):

$$\boldsymbol{\theta} \sim MVN(\mathbf{0}, \mathbf{Q}^{-1}(\boldsymbol{\psi}))$$

The Markov property ensures the sparsity of the precision matrix \mathbf{Q} .

The aim of Bayesian inference is to obtain the posterior marginal distributions for all the model parameters $p(\theta_i|\mathbf{y}) = \int p(\theta_i, \boldsymbol{\psi}|\mathbf{y})d\boldsymbol{\psi} = \int p(\theta_i|\boldsymbol{\psi}, \mathbf{y})p(\boldsymbol{\psi}|\mathbf{y})d\boldsymbol{\psi}$ and hyperparameters $p(\psi_k|\mathbf{y}) = \int p(\boldsymbol{\psi}|\mathbf{y})d\boldsymbol{\psi}_{-k}$.

Therefore we first need to compute (i) the joint posterior marginal of the hyperparameters $p(\boldsymbol{\psi}|\mathbf{y})$ and (ii) the posterior conditional distributions $p(\theta_i|\boldsymbol{\psi}, \mathbf{y})$.

Within such class of models, which includes a wide range of possible model specifications, we can compute these distributions through a Laplace approximation:

$$\begin{aligned} p(\boldsymbol{\psi}|\mathbf{y}) &= \frac{p(\boldsymbol{\theta}, \boldsymbol{\psi}|\mathbf{y})}{p(\boldsymbol{\theta}|\boldsymbol{\psi}, \mathbf{y})} = \frac{p(\mathbf{y}|\boldsymbol{\theta}, \boldsymbol{\psi})p(\boldsymbol{\theta}, \boldsymbol{\psi})}{p(\mathbf{y})} \frac{1}{p(\boldsymbol{\theta}|\boldsymbol{\psi}, \mathbf{y})} \propto \frac{p(\mathbf{y}|\boldsymbol{\theta}, \boldsymbol{\psi})p(\boldsymbol{\theta}, \boldsymbol{\psi})}{p(\boldsymbol{\theta}|\boldsymbol{\psi}, \mathbf{y})} \\ &\approx \frac{p(\mathbf{y}|\boldsymbol{\theta}, \boldsymbol{\psi})p(\boldsymbol{\theta}, \boldsymbol{\psi})}{\tilde{p}(\boldsymbol{\theta}|\boldsymbol{\psi}, \mathbf{y})} \Big|_{\boldsymbol{\theta}=\boldsymbol{\theta}^*(\boldsymbol{\psi})} =: \tilde{p}(\boldsymbol{\psi}|\mathbf{y}) \end{aligned}$$

where $\tilde{p}(\boldsymbol{\theta}|\boldsymbol{\psi}, \mathbf{y})$ is the Gaussian Laplace approximation of $p(\boldsymbol{\theta}|\boldsymbol{\psi}, \mathbf{y})$ around its mode $\boldsymbol{\theta}^*(\boldsymbol{\psi})$.

For $p(\theta_i|\boldsymbol{\psi}, \mathbf{y})$ we consider a partition $\boldsymbol{\theta} = (\theta_i, \boldsymbol{\theta}_{-i})$:

$$\begin{aligned} p(\theta_i|\boldsymbol{\psi}, \mathbf{y}) &= \frac{p((\theta_i, \boldsymbol{\theta}_{-i})|\boldsymbol{\psi}, \mathbf{y})}{p(\boldsymbol{\theta}_{-i}|\theta_i, \boldsymbol{\psi}, \mathbf{y})} = \frac{p(\boldsymbol{\theta}, \boldsymbol{\psi}|\mathbf{y})}{p(\boldsymbol{\psi}|\mathbf{y})} \frac{1}{p(\boldsymbol{\theta}_{-i}|\theta_i, \boldsymbol{\psi}, \mathbf{y})} \propto \frac{p(\boldsymbol{\theta}, \boldsymbol{\psi}|\mathbf{y})}{p(\boldsymbol{\theta}_{-i}|\theta_i, \boldsymbol{\psi}, \mathbf{y})} \\ &\approx \frac{p(\boldsymbol{\theta}, \boldsymbol{\psi}|\mathbf{y})}{\tilde{p}(\boldsymbol{\theta}_{-i}|\theta_i, \boldsymbol{\psi}, \mathbf{y})} \Big|_{\boldsymbol{\theta}_{-i}=\boldsymbol{\theta}_{-i}^*(\theta_i, \boldsymbol{\psi})} =: \tilde{p}(\theta_i|\boldsymbol{\psi}, \mathbf{y}) \end{aligned}$$

where $\tilde{p}(\theta_i|\boldsymbol{\psi}, \mathbf{y})$ is the Gaussian Laplace approximation of $p(\theta_i|\boldsymbol{\psi}, \mathbf{y})$ around its mode $\boldsymbol{\theta}_{-i}^*(\theta_i, \boldsymbol{\psi})$.

In R-INLA other approximation strategies are implemented and can be chosen to speed up the computation.

In particular, $p(\theta_i|\boldsymbol{\psi}, \mathbf{y})$ can be directly derived from the Normal approximation $\tilde{p}(\boldsymbol{\theta}|\boldsymbol{\psi}, \mathbf{y})$ already computed in the first step (Gaussian strategy). This can produce inaccurate approximations, however when the conditional $p(\theta|\boldsymbol{\psi}, \mathbf{y})$ is Gaussian it is an exact approximation and there is no need to apply the Laplace method, as in our case.

For point-referenced data (i.e. data observed at point locations typically referenced by coordinates), the latent continuous spatial process is a Gaussian Field (GF) with dense spatial covariance matrix that leads to computational issues. The SPDE approach proposed by Lindgren *et al.* (2011) is an alternative which consists in representing a continuous spatial process (the GF) as a discretely indexed spatial random process (i.e. a GMRF).

The continuous GF with Matérn covariance structure $z(\mathbf{s})$ is the exact and stationary solution of the following stochastic partial differential equation:

$$(\kappa^2 - \Delta)^{\alpha/2}(\tau z(\mathbf{s})) = \mathcal{W}(\mathbf{s}) \quad (1)$$

where Δ is the Laplacian, α is a smoothness parameter, κ is a scale parameter, τ controls the variance, \mathbf{s} is the generic spatial location and $\mathcal{W}(\mathbf{s})$ is a Gaussian spatial white noise process.

For the relationship between the SPDE in Eq. (1) and the Matérn parameters see Eq. (2) in Appendix D.

For details on how to solve the SPDE that gives a Matérn random field see Bakka (2018).

This solution $z(\mathbf{s})$ can be approximated through a weighted sum of basis functions ψ_g defined at the G vertices (nodes) of a triangulation (mesh) of the domain with zero-mean Gaussian-distributed weights \tilde{z}_g (Lindgren *et al.*, 2011):

$$z(\mathbf{s}) = \sum_{g=1}^G \psi_g(\mathbf{s}) \tilde{z}_g$$

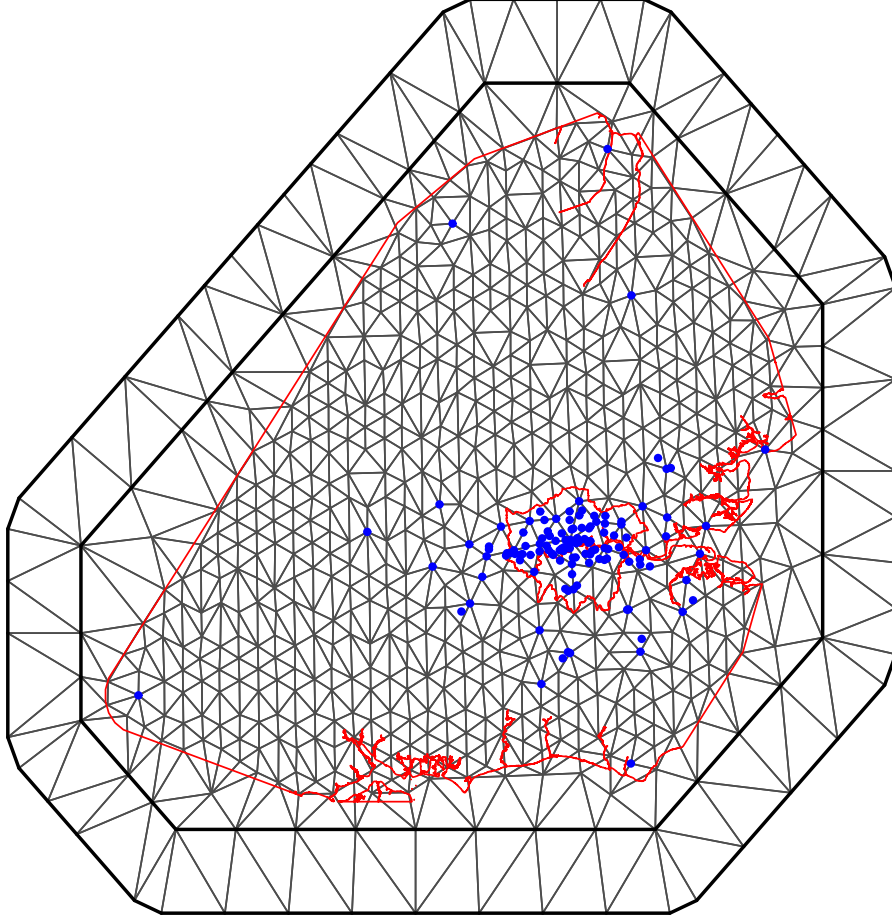


Figure C.1: Domain triangulation (mesh) with 686 vertices (nodes). The red lines are the boundaries of Greater London and the south-eastern coast of UK representing the study area. The blue dots are the locations of the monitoring stations.

Therefore, at a discrete set of locations $\mathbf{s}_0 = (s_1, \dots, s_G)$, i.e. the mesh nodes, the GP \mathbf{z} follows a multivariate Normal distribution with zero mean and spatially structured correlation matrix.

Figure C.1 shows the mesh constructed on our data.

At the data locations we write $z_i = Az(s_0)$ where A is the projection matrix from the mesh nodes to the data locations. This simplifies the notation as the distribution assumed at the data locations has a complicated form.

D Matérn covariance function and INLA-SPDE

Let $r = d(i, j) = \|s_i - s_j\|$ for two-dimensional domains. Then the Matérn class of stationary and isotropic covariance functions is defined as

$$COV(r) = \frac{\sigma^2}{\Gamma(\lambda)2^{\lambda-1}} (\kappa r)^\lambda K_\lambda(\kappa r) \quad (2)$$

where $\sigma^2 = \frac{\Gamma(\lambda)}{\Gamma(\alpha)(4\pi)^{d/2}\kappa^{2\lambda}\tau^2}$ is the marginal variance, K_λ is the modified Bessel function of second kind and order $\lambda > 0$, $\lambda = \alpha - d/2$ is a smoothness parameter, where d is the dimension of the domain (2 in case of spatial processes). We refer the reader to Lindgren and Rue (2015) for a discussion on the choice of α implemented in R-INLA. Finally, κ is a scaling parameter related to the empirically derived range $\rho = \sqrt{8\lambda}/\kappa$.

We adopt the default $\alpha = 2$, which for two-dimensional domains means smoothness parameter $\lambda = 1$.

We need a parameterization to represent the Matérn correlation structure in INLA. The easiest way would be to assign a joint normal prior distribution to $\psi_1 = \log(\tau)$ and $\psi_2 = \log(\kappa)$, in fact from the formula of the marginal variance σ^2 we can derive

$$\log(\tau) = \frac{1}{2} \log \left(\frac{\Gamma(\lambda)}{\Gamma(\alpha)(4\pi)^{d/2}} \right) - \log(\sigma) - \lambda \log(\kappa) \quad (3)$$

and from the formula of the empirical range $\rho = \sqrt{8\lambda}/\kappa$ we obtain

$$\log(\kappa) = \frac{1}{2} \log(8\lambda) - \log(\rho) \quad (4)$$

A more naturally interpretable parameterization is in terms of standard deviation σ and range ρ , such as

$$\log(\sigma) = \log(\sigma_0) + \psi_1 \quad (5)$$

$$\log(\rho) = \log(\rho_0) + \psi_2 \quad (6)$$

Substituting (5) in (3) and (6) in (4) we get respectively:

$$\log(\tau) = \log(\tau_0) - \psi_1 - \lambda \log(\kappa) \quad (7)$$

$$\log(\kappa) = \log(\kappa_0) - \psi_2 \quad (8)$$

from which

$$\log(\tau) = \log(\tau_0) - \psi_1 - \lambda \psi_2 \quad (9)$$

$$\log(\kappa) = \log(\kappa_0) - \psi_2 \quad (10)$$

so we can express τ and κ in terms of ψ_1 and ψ_2 (Lindgren and Rue, 2015).

More recently, Fuglstad *et al.* (2019) suggested an extension of the penalized complexity prior (PC prior) proposed by Simpson *et al.* (2017). The PC prior penalizes the Kullback-Liebler divergence between the model P and the base model P_0 , i.e. the information lost when approximating P with P_0 , and it is suggested as a way to reduce overfitting. Here P represents a model component, such as a GRF.

Fuglstad *et al.* (2019) developed a joint version of the PC prior for the range and marginal variance of Matérn GRFs with fixed smoothness and $d < 4$. The joint PC prior is derived from the alternative parameterization of the Matérn covariance function (τ, κ) and then transformed back on the range and variance scale (ρ, σ) . The advantage of PC priors compared to the prior described above is that it can be expressed in a user friendly form stating the upper or lower tail probability for the generic parameter of interest ϕ : $P(\phi > U) = q$ or $P(\phi < L) = q$. This intuitive interpretation makes it easy to specify a vague, weak or informative prior by tuning the parameter.

In the case of the joint PC prior for GRFs, we must choose an upper limit for the standard deviation and a lower limit for the range: $P(\sigma > \sigma_0) = q_1$ and $P(\rho < \rho_0) = q_2$.

E Implementation of the joint model through the INLA-SPDE approach

Because we have misaligned data, we describe the joint model with three likelihoods and three linear predictors (section 3.2, equations 1, 2, 3).

To implement this in R-INLA, we need to create a complex data structure: the matrix of observations M is defined as a block matrix with the number of columns corresponding to the number of likelihoods and each block row corresponding to the data used to estimate one of the linear predictors (Martins *et al.*, 2013).

$$M = \begin{pmatrix} \begin{pmatrix} y_1(1, 1) \\ \vdots \\ y_1(s_1, t_1) \end{pmatrix} & \mathbf{NA} & \mathbf{NA} \\ \mathbf{NA} & \begin{pmatrix} y_2(1, 1) \\ \vdots \\ y_2(s_2, t_2) \end{pmatrix} & \mathbf{NA} \\ \mathbf{NA} & \mathbf{NA} & \begin{pmatrix} y_3(1, 1) \\ \vdots \\ y_3(s_3, t_2) \end{pmatrix} \end{pmatrix}$$

The dimension of M is then $(s_1 t_1 + s_2 t_2 + s_3 t_2) \times 3$, with $s_1 = 44117$ PCM grid cells, $s_2 = 495$ AQUM grid cells, $s_3 = 124$ monitoring stations, $t_1 = 5$ years, $t_2 = 1826$ days.

Through the `R-INLA copy` function, the z_1 and z_2 random effects are included in the linear predictor, so each of them shares the hyperparameters across the linear predictors in eq. 1-3, but at the same time has a scaling parameter as well for calibration purposes (Gómez-Rubio, 2019; Rue *et al.*, 2017).

Since the SPDE provides the approximation of the entire spatial process at the mesh nodes, there is no actual alignment procedure involved here. For the blocks with spatial structure (all three in our case), we just need a link between the mesh nodes and the locations at which the value is known; this link is provided by a projector matrix defined by built-in functions. Because these locations are different, we need one projector matrix for the PCM data y_1 , one for the AQUM data y_2 and one for the ground observations y_3 .

For each block, a R-INLA stack object is created to link the data and/or the projector matrix to the model effects included in the linear predictor: for the y_1 stack we will have the intercept and only one random effect represented by the spatial index, for y_2 we have the intercept, a temporal and a spatial index, and for y_3 we will need the intercept, the site type covariate, the spatial index for z_1 , the temporal index for z_2 and the time-site type interaction for z_3 .

All the stack objects are then put together and passed on to the `inla` call as data.

With this data structure it is easy to include a validation set: assuming we select m sites for validation and the remaining $n = s_3 - m$ for estimation, we just need to set the observations corresponding to the validation locations to *NA*, so that R-INLA will assume them as unknown and will predict their values. In this case the M matrix will be:

$$M = \begin{pmatrix} \begin{pmatrix} y_1(1, 1) \\ \vdots \\ y_1(s_1, t_1) \end{pmatrix} & \mathbf{NA} & \mathbf{NA} \\ \mathbf{NA} & \begin{pmatrix} y_2(1, 1) \\ \vdots \\ y_2(s_2, t_2) \end{pmatrix} & \mathbf{NA} \\ \mathbf{NA} & \mathbf{NA} & \begin{pmatrix} y_3(1, 1) \\ \vdots \\ y_3(n, t_2) \\ NA(n+1, 1) \\ \vdots \\ NA(n+m, t_2) \end{pmatrix} \end{pmatrix}$$

We also need the projector matrix associated with the validation set and the corresponding stack object. The prediction is computed at each new location (either a validation site or on a regular grid) through the procedure described in Section 3.5.

F Retrieving site type at unknown locations

To determine the site type at unknown locations, we tested 12 different approaches on the known monitoring sites using four different land cover sources of information to retrieve the rural and urban classification, and three different rules to

Table F.1: Accuracy of methods to retrieve site type based on the 126 known monitors.

Land use	R1	R2	R3
Corine	43.2%	63.2%	64.8%
MODIS	39.2%	60.8%	64.0%
GUF 1km	37.6%	58.4%	62.4%
GUF 12m	39.2%	60.8%	63.2%

determine the road-kerb side classification based on the distance from a major or minor road (Greater London Ordnance Survey minor and major roads ESRI shapefile - Ordnance Survey 2017).

The first source for land cover is the Corine land cover for the year 2012 for the UK, Jersey and Guernsey shapefile from the Centre for Ecology and Hydrology (Cole *et al.*, 2015), the second is the MODIS land cover type 1 classification raster at 500m resolution for year 2005 from NASA LP DAAC (2013), and the last two are the Global Urban Footprint (GUF) rasters at 1km and 12m resolution respectively (DLR, 2016; Esch *et al.*, 2017). In all cases, the non-urban land cover types are aggregated to rural, and we assume the land cover did not change significantly over the study period.

We applied the following three rules to all the land cover data:

(R1) The site type is defined as road-kerb side if the location is within 4 m from any road, otherwise urban or rural according to the land cover shapefile. This rule combined with the MODIS land cover is the one applied by Mukhopadhyay and Sahu (2017).

(R2) The site type is defined as road-kerb side if the location is within 10 m from any road, otherwise urban or rural according to the landcover shapefile.

(R3) The site type is defined as road-kerb side if the location is within 50 m from a major road or within 10 m from a minor road, otherwise urban or rural according to the landcover shapefile. This rule accounts for the different width of the roads, assuming the road midline corresponds to the center of the street.

The percentage of correctly classified monitors for each method is reported in Table F.1.

The Corine shapefile seems to provide more accurate information compared to the MODIS raster, and combined with the 10/50m rule it gives the highest percentage of correct classification (64.8%). This method was therefore applied to the unknown locations.

G Code

The code is available on the GitHub repository https://github.com/cf416/joint_model_no2.

The data workspace can be requested directly to the corresponding author.